Towards Quantitative Nanothermometry Using Single-Molecule Counting

Phillip A. Reinhardt, Abigail P. Crawford, Claire A. West, Gabe Delong, Stephan Link, David J. Masiello, Katherine A. Willets*

Department of Chemistry, Temple University, Philadelphia, Pennsylvania 19122, United States

Department of Chemistry, University of Washington, Seattle, Washington 98195, United States

Department of Chemistry, Department of Electrical and Computer Engineering, Rice University,

Houston, Texas 77005, United States

KEYWORDS Super-resolution imaging, plasmon, nanothermometry, DNA-PAINT, single molecule, fluorophore, photothermal heating

ABSTRACT Photothermal heating of nanoparticles has applications in nanomedicine, photocatalysis, photoelectrochemistry, and data storage, but accurate measurements of temperature at the nanoparticle surface are lacking. Here we demonstrate progress towards a superresolution DNA nanothermometry technique capable of reporting the surface temperature on single plasmonic nanoparticles. Gold nanoparticles are functionalized with double-stranded DNA, and the extent of DNA denaturation under heating conditions serves as a reporter of temperature. Fluorescently-labeled DNA oligomers are used to probe the denatured DNA through transient binding interactions. By counting the number of fluorescent binding events as a function of

temperature, we reconstruct DNA melting curves that reproduce trends seen for solution-phase DNA. Further, we demonstrate our ability to control the temperature of denaturation by changing Na⁺ concentration and the base pair length of the double-stranded DNA on the nanoparticle surface. This degree of control allows us to select narrow temperature windows to probe, providing quantitative measurements of temperature at nanoscale surfaces.

INTRODUCTION

Noble metal nanoparticles have attracted significant interest due to their ability to support localized surface plasmons, which not only allow for efficient harvesting of photon energy, but also its conversion into other forms, such as chemical and thermal energy. ^{1–3} By converting photon energy to thermal energy, plasmonic nanoparticles effectively become nanoscale heat sources, increasing the local temperature at their surface by many tens of degrees. ^{4–7} The ability to provide nanolocalized heating has been utilized across a diverse array of applications, including heat-assisted magnetic recording, ^{8–10} photothermal therapy, ^{11–13} drug delivery, ^{14–16} photocatalysis, ^{17–20} and photoelectrochemistry. ^{21–23} However, one challenge with using nanoparticles as localized heat sources is that it is difficult to monitor the temperature directly at the nanoparticle surface, given their small size (typically less than 500 nm) and spatially-confined thermal profiles.

Currently, there are several strategies for performing nanothermometry on plasmonic nanoparticles. For example, multiple groups have used the ratio between Stokes and anti-Stokes gold photoluminescence as a method to calculate the internal temperature of individual gold nanoparticles.^{24,25} Others have used the ratio of Stokes to anti-Stokes surface-enhanced Raman scattering (SERS) from reporter molecules adsorbed to plasmonic nanoparticles to calculate the temperature experienced by molecules at the surface.^{26,27} The latter approach offers the advantage

of reporting more directly on the local environment at the surface of the nanoparticles (where reactions and other thermally-mediated processes occur), but it suffers from the need to account for differences in the SERS electromagnetic enhancement of the two different vibrational modes, complicating the analysis.²⁸ Moreover, both techniques require the system to generate sufficiently strong luminescence or SERS signals. While this is often—though not always—true for plasmonic metals, the approaches are not broadly generalizable to other classes of nanoparticles.

Alternative strategies for nanothermometry use temperature-dependent properties of fluorescent molecules to report on local temperature. For example, temperature can increase the non-radiative decay rate of some fluorophores, which results in a decrease in both lifetime and fluorescence intensity at elevated temperatures.²⁹ The diffusion coefficient of free dyes in solution is also temperature-dependent, which can be measured by fluorescence correlation spectroscopy and used to infer temperature within the excitation volume.²⁹ Others have used temperature-dependent DNA hairpin loops which change the distance between a fluorophore-quencher pair or fluorophore-fluorophore pair depending on whether the hairpin loop is open (at high temperature) or closed (at low temperature). ^{30–34} Temperature-dependent changes in distance are read out through changes in fluorescence intensity, which are a byproduct of either fluorophore quenching or Förster resonance energy transfer. Other approaches measure the release of fluorophore-modified DNA from the surface of photothermally-heated plasmonic nanoparticles, either through denaturation or the breakage of the Au-thiolate bond, yielding an ensemble averaged temperature experienced by the nanoparticles.^{35,36}

All the optical techniques described thus far are inherently limited by the diffraction limit of light, which caps the spatial resolution of optical images to roughly half the optical wavelength. While this limited spatial resolution is not problematic when characterizing the temperature of a

well-isolated single nanoparticle, it becomes more complicated for nanoparticle assemblies, where local thermal differences may exist.^{37–39} For example, our recent work showed that nanorod dimers and trimers are able to localize heat to specific particles within the assembly, creating nanoscale thermal gradients that are actively controllable by changing the excitation wavelength.^{38,39} By analyzing distortions in the diffraction-limited point spread functions of photothermal images, we were able to experimentally validate thermal confinement, but not measure the local temperature directly on individual nanorods within the structures. Thus, for multi-particle assemblies, it would be useful to have a nanothermometry technique that is able to both defeat the diffraction limit of light as well as provide quantitative temperature measurements to probe local temperature differences.

Herein, we present the first steps towards a super-resolution fluorescence imaging technique capable of single-particle thermal measurements with sub-diffraction-limited resolution. **Figure 1A** illustrates the basic principle. Gold nanoparticles are functionalized with thiolated single stranded DNA (ssDNA), known as the anchor strand. The anchor is then hybridized to a complementary strand of DNA, known as the blocking strand. The hybridization status of the anchor strand can be determined by DNA-PAINT (point accumulation for imaging nanoscale topography), using short oligomers of fluorophore-labeled ssDNA, known as imaging strand, that are complementary to the terminal sequence of the anchor strand. 40,41 Upon binding of the imaging strand to any available anchor strand, a burst of fluorescence occurs and is counted. At temperatures below the melting temperature (T_m) of the anchor + blocking DNA duplex, no anchor strand is available for binding, resulting in low numbers of fluorescent events associated with the imaging strand (**Figure 1A**, **left**). If the sample is exposed to temperatures well above the T_m of the duplex, all blocking strands will melt, resulting in a maximum number of fluorescent binding

events between the anchor and the imaging strand (**Figure 1A, right**). If the temperature $T \approx T_m$ of the duplex, roughly half of the blocking strands will be removed, resulting in intermediate fluorescence activity (**Figure 1A, middle**). By counting the number of fluorescence events as a function of temperature, we generate a DNA melting curve that follows the expected sigmoidal DNA denaturation profile (**Figure 1B**). The T_m of the anchor + blocking duplex can be tuned by changing the length of the blocking strand and/or the salinity of the buffer solution, allowing us to tune the sensitivity of our nanothermometer into various temperature regimes. Moreover, by fitting each fluorescence event to a 2-dimensional Gaussian function, we are able to reconstruct the underlying structure of the gold nanoparticle substrate with sub-diffraction-limited resolution. Thus, our approach offers both quantitative nanoscale temperature measurements as well as the ability to map thermal differences on <20 nm length scales.

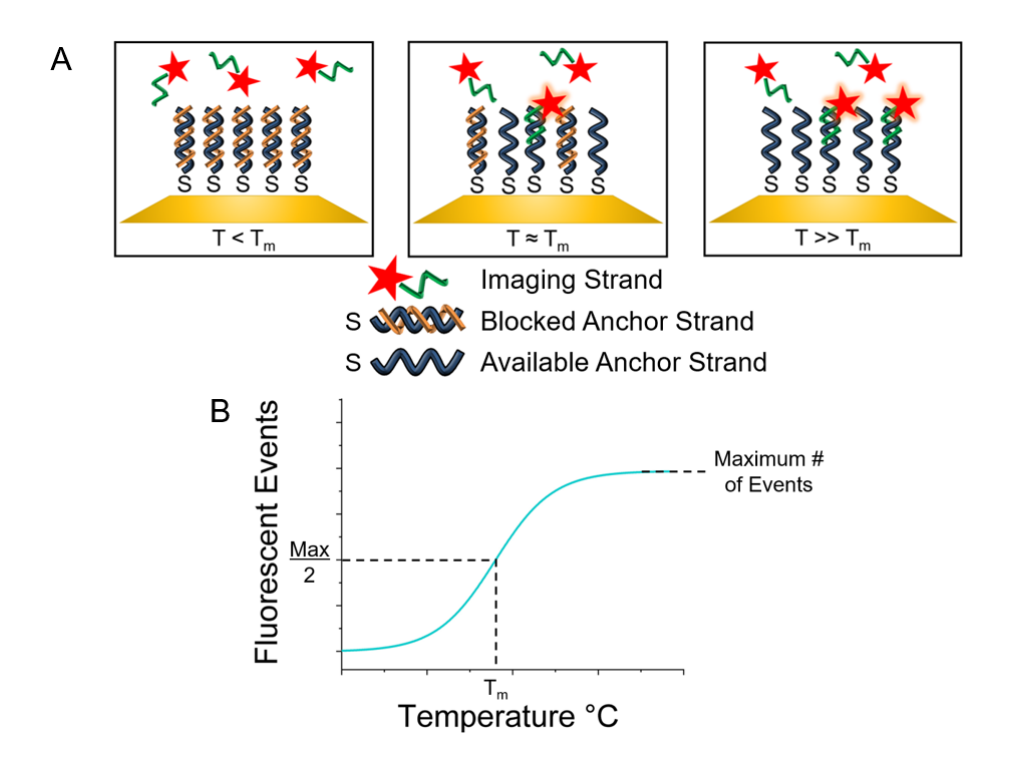


Figure 1: (A) Schematic of DNA-PAINT nanothermometry experiments. (Left) Gold nanoparticles are functionalized with thiolated anchor strand (blue) which is then hybridized to its complement (the "blocking" strand, orange), creating double stranded DNA. Fluorophore-labeled

imaging strand (green with red star) is unable to interact with the surface-bound anchor strand due to the presence of the blocking strand. (Middle) When $T \approx T_m$, ~50% of the blocking strand denatures, leaving exposed anchor strands to interact with imaging strands. Upon binding to an anchor strand, each imaging strand generates a measurable burst of fluorescence. (Right) When $T \gg T_m$, all blocking strand is removed, generating an increase in the number of measured fluorescence events associated with transiently bound imaging strand. (B) A schematic melting curve using this technique, showing how the fluorescent events associated with imaging strand binding are expected to increase as a function of temperature. The number of events can be normalized to the maximum number of events and fit to a sigmoid, allowing T_m to be extracted.

METHODS

Substrate Preparation: Complete details of the substrate preparation and DNA functionalization steps can be found in the Supporting Information. Briefly, periodic arrays of gold nanotriangles were prepared using nanosphere lithography on #1 thickness glass coverslips. 42 After cleaning, a SecureSeal hybridization chamber from Grace Bio-Labs was adhered to the substrate. The nanoparticles were functionalized with a 48 base pair (BP) thiolated single-stranded DNA (anchor strand) using a modified low-pH, high salt method. 43,44 After anchor strand functionalization, the sample was heated to 58°C in 0.3X phosphate buffered saline (PBS) to promote a more uniform DNA monolayer, based on our previous work. 45 For a "blocked" sample, complementary 36 or 24 BP strand (blocking strand) was hybridized to the anchor strand by slow heating and cooling. Sample Heating: All sample heating was performed ex situ on a hot plate, followed by imaging at room temperature. For the ex situ heating, DNA-functionalized samples were placed in petri dishes floating on a thermocouple-controlled water bath (see Figure S1). The hybridization chambers are filled with pre-heated buffer at the desired temperature. A reference sample with an embedded thermocouple provided direct temperature measurements of the nanoparticle environment, allowing us to monitor any differences between the water bath temperature and the temperature at the substrate. After heating, the warm buffer solution was removed and samples

were rinsed with room temperature buffer before being transferred to the microscope to be imaged at room temperature.

Fluorescence Imaging: The imaging solution consisted of short strands of DNA (10 or 12 BP) modified with Atto532 dye (imaging strand) in 2.0X PBS + 600 mM NaCl. Samples were imaged on an inverted microscope with a 100x oil-immersion objective and excited by a 532 nm laser in a total internal reflection configuration (Figure S2). The emission passed through a bandpass filter to a CCD camera, which collected movies for 1000 frames with a 200 ms integration time. The bandpass filter at 575 nm was used to reject background luminescence from the gold nanoparticles. The full experimental setup and additional details can be found in the Supporting Information.

For each imaging experiment, we moved to a different region of interest on the sample. This allowed us to build up statistics on different regions to validate the robustness of our imaging strategy, while also avoiding potential degradation of the DNA due to the formation of reactive oxygen species. We observed some loss of activity after imaging the same region for long periods of time, although we could minimize the effect by introducing oxygen scavengers (*vide infra*); however, for the work presented here, we chose to image different regions in order to generate statistics and demonstrate site-to-site reproducibility. Introducing oxygen scavengers and/or a flow cell will help alleviate this issue in future implementations of this approach.

Image Processing: The 1000 frame movies were cropped and processed using open-source MATLAB Code Small-Labs.⁴⁷ This software is designed to account for high background systems and to accurately count true DNA binding events based on intensity, duration, and quality of fit while rejecting short-lived non-specific binding events (see Supporting Information for additional detail). We used the same analysis parameters for all experiments described in the text, allowing the code to determine fluorescence events, in order to prevent any researcher-dependent biases.

RESULTS

For our experiments, we fabricated periodic arrays of gold nanotriangles using nanosphere lithography. Figure 2A shows a representative atomic force microscopy image of a nanoparticle array produced by this technique, with nanotriangles that measure ~210 nm from base-to-tip. For comparison, Figure 2B shows a super-resolved DNA-PAINT image, demonstrating that we are able to recreate the expected pattern and shape of the nanotriangles. The DNA-PAINT experiments were performed on gold nanotriangles functionalized with only anchor strand and imaged with a 12 BP imaging strand solution. The resulting image not only reveals that we have uniform binding of the anchor strand to the gold nanoparticles, but also that we only localized imaging strand at the particle surface, indicating that non-specific binding between nanoparticles was not an issue. Moreover, the size of the nanotriangles were below the diffraction limit of light, confirming that our DNA-PAINT approach provided the requisite spatial resolution to map individual nanoparticles within an assembly. ³⁹

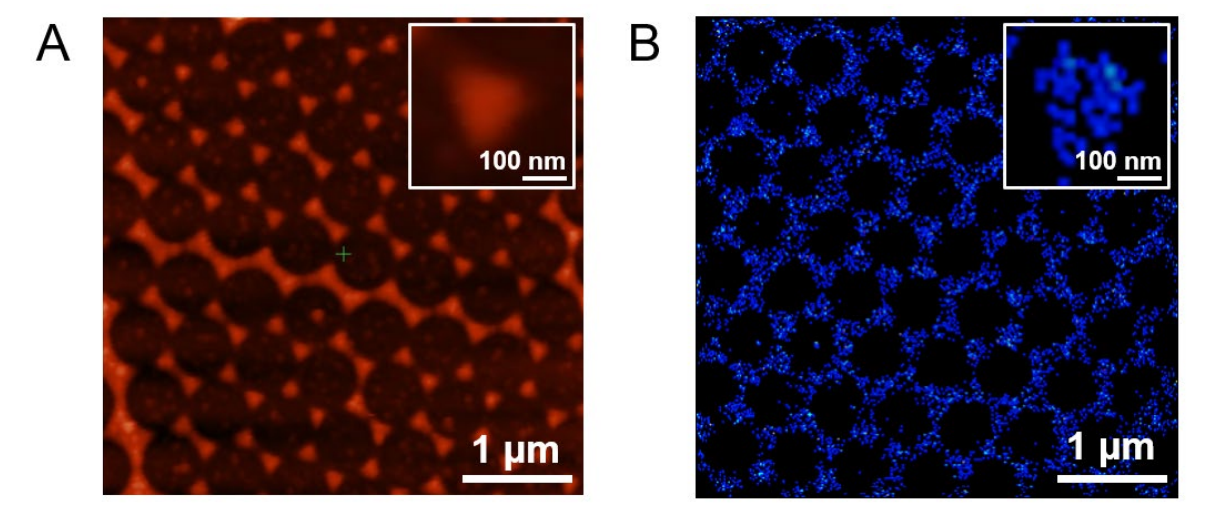


Figure 2: (A) Atomic Force Microscopy image showing a representative gold nanoparticle array created using nanosphere lithography. (B) Super-resolved DNA-PAINT image of a representative gold nanoparticle array, created by localizing fluorescent events associated with imaging strands interacting with anchor strands on the surface of the gold nanotriangles. The inset of both figures

is a zoomed-in image of a single triangular nanoparticle. The super-resolved data was generated by acquiring 5000 image frames with a 200 ms integration time.

Having demonstrated successful mapping of exposed anchor strands by DNA-PAINT, we next tested the ability of the blocking strand to prevent interactions between the imaging strand and the anchor (as in **Figure 1A**, left). **Figure 3** shows the number of fluorescent events associated with a sample in which the anchor strands were blocked with a 36 BP complement (leftmost bar). The mean number of fluorescent binding events between the imaging strand and the anchor was at or near background, showcasing the effective hybridization between the surface tethered anchor strand and the blocking strand. Moreover, the low number of binding events for the blocked sample validated that the laser used during DNA-PAINT imaging did not result in any appreciable photothermal heating of the nanoparticles, as we would expect to see the number of fluorescence events to continuously increase above background if the laser were driving any photothermal processes (e.g. DNA melting) at the surface. This conclusion was further supported by calculations that show that our laser is far from the absorption resonance of the nanotriangles (**Figure S3A**), leading to minimal heating at the surface (**Figure S3B**).

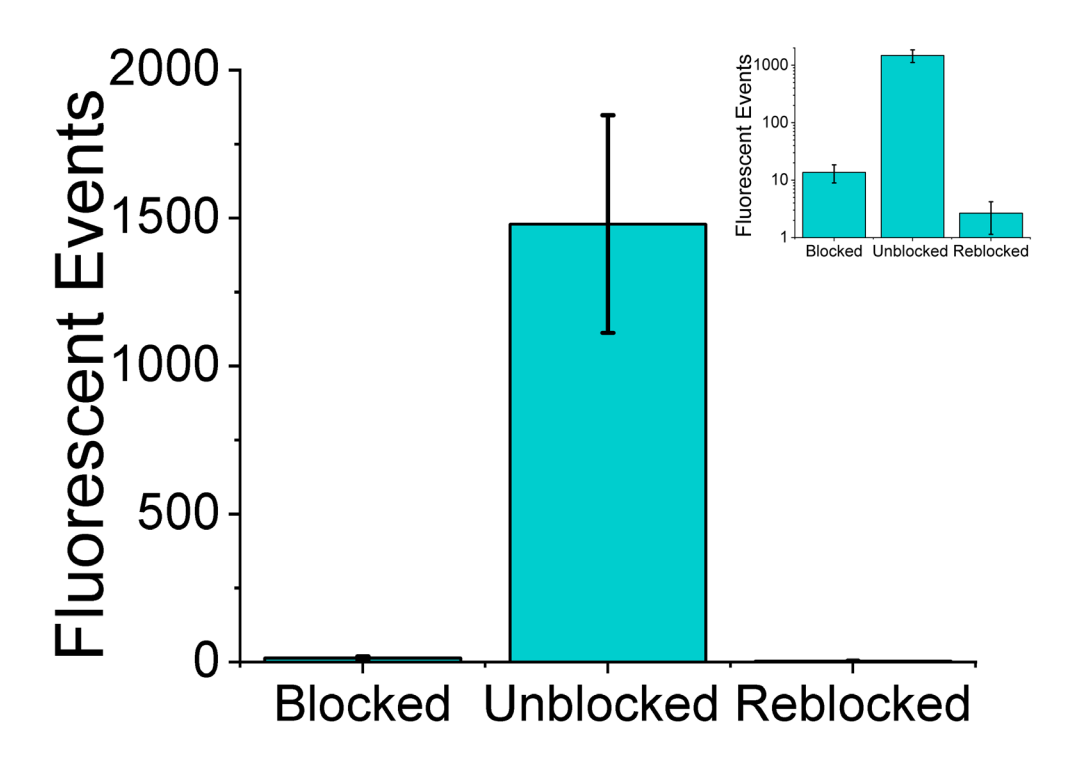


Figure 3: Fluorescence counts as a function of the hybridization status of the 48 BP anchor strand. The sample started off blocked by its 36 BP complement, resulting in a low number of fluorescent events when the imaging strand was introduced (left bar). After heating to ~58°C for 20 minutes, significant fluorescent events from the imaging strand is observed, indicating successful removal of the blocking strand (center bar). Reintroduction of the blocking strand restores the low number of fluorescent binding activity (right bar). Error bars represent the standard deviation across three repeat measurements at different regions of interest on the sample (note that the error bars are too small to be seen for the blocked cases). Inset shows the same data on a log scale.

Next, we performed $ex \, situ$ heating of the sample for 20 minutes at 58°C, which is higher than the predicted T_m of 54°C for the duplex between our 48 BP anchor strand and 36 BP blocking strand. After heating, the sample was cooled to room temperature and imaged on the microscope. The total number of fluorescence events increased dramatically (**Figure 3**), indicating that we successfully removed all or nearly all of the blocking strand from the surface. Lastly, we reintroduced blocking strand to the sample (See supporting information for heating and cooling

method) and found that we could successfully re-block the sample and return to a low number of fluorescent events. Based on the comparison between the fluorescence activity of the blocked and unblocked samples, we calculate the hybridization efficiency between the anchor strand and the blocking strand to be 99.1 +/- 0.4 %. These results demonstrate reversible control over the DNA-PAINT activity depending upon the hybridization status of the anchor strand.

Our next control tested the surface-tethered duplex stability to ensure our results were not affected by the length of time that the sample was heated. Figure 4 shows the number of fluorescence events measured for a sample exposed to multiple ex situ heating cycles at 37°C, with fully blocked and fully unblocked signals shown for comparison (leftmost and rightmost bars, respectively). For these data, the sample was blocked with a 24 BP complement and imaged with a 12 BP imaging strand, initially resulting in very little fluorescent activity. The sample was then heated at 37°C in 0.6X PBS for 10 minutes before imaging, resulting in an increase in fluorescent counts that shows duplex melting occurred. The sample was then subjected to another 10 minutes at 37°C and maintained a very similar number of fluorescent binding events, showing that the number of exposed anchor strands did not appreciably change, even with the additional heating step. This procedure was repeated for a third 10-minute heating cycle, and similar counts were observed. F-tests confirmed that the differences in counts were not statistically significant. If subsequent heating cycles were leading to additional DNA melting, we would expect the fluorescence counts to increase with each exposure at 37°C; instead, we observed a fairly flat response, indicating that the number of counts is dominated by the thermodynamics of the system. To confirm that we were not in a regime in which all duplexes were melted, we heated the sample to 58°C for 20 minutes in 0.6X PBS, which is sufficient to melt off the remainder of the blocking strand, and found that the activity was roughly double the activity seen at 37°C. This difference

between counts at 37°C and 58°C validated that the fluorescence counts were sensitive to the hybridization status (and thus temperature) of the system. **Figure S4** shows a second stability test under different conditions to further strengthen our argument that the timescale of heating had a minimal effect on the measured counts. We note that 10 minutes is an upper bound on the length of time required to melt the DNA duplexes; future work will probe the temporal dependence in more detail.

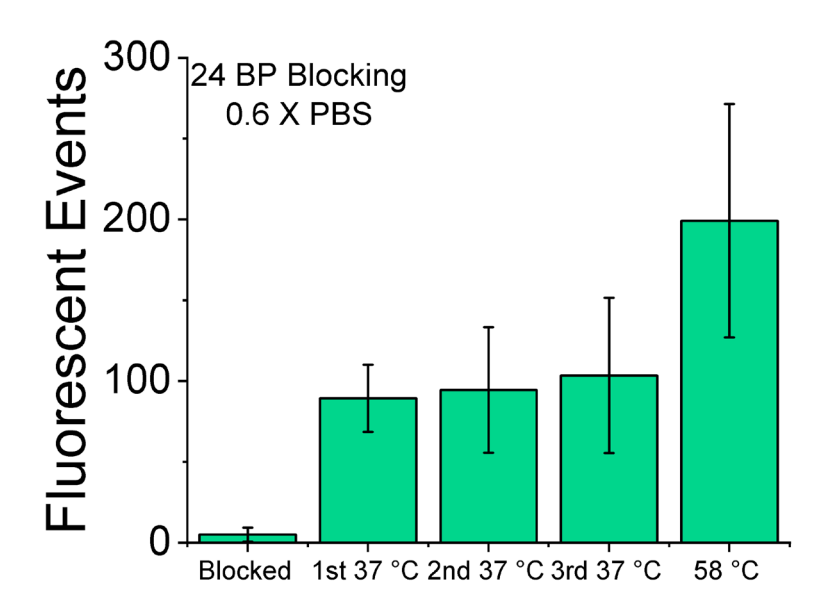


Figure 4: Stability test showing that repeated heating cycles maintain uniform activity levels. The sample was blocked with a 24 BP blocking strand, heated at ~37°C three times for ten minutes each, and then heated to 58°C for 20 minutes to fully remove the blocking strand. The sample was imaged with a 12 BP imaging strand between each heating cycle. Data points reflect the average of three repeat measurements at different regions of interest on the same sample, with the error bars representing the standard deviation across those three measurements.

Having established the robustness of our approach to report on differences in temperature, we next optimized the length and concentration of the imaging strand in order to maximize the number of counts for the fully unblocked sample. **Figure 5** shows the number of fluorescent events

generated on a fully unblocked sample using either a 10 or 12 BP imaging strand at different concentrations in a 2.0X PBS + 600 mM NaCl imaging buffer. As expected, the 10 BP imaging strand had higher total event counts than the 12 BP due to its lower predicted T_m (30.8°C vs 41.5°C) and thus shorter interaction time with the anchor strand. Both sets of data show that the fluorescence activity saturates at high concentration of imaging strand due to spatial and temporal overlap of binding events that prevent accurate counting. From these curves, we chose 10 pM of the 10 BP imaging strand as our ideal concentration, as these conditions maximized binding events while still maintaining accurate counting statistics. Moreover, this concentration ensured that we record sufficient counts at intermediate temperatures when the sample is partially blocked.

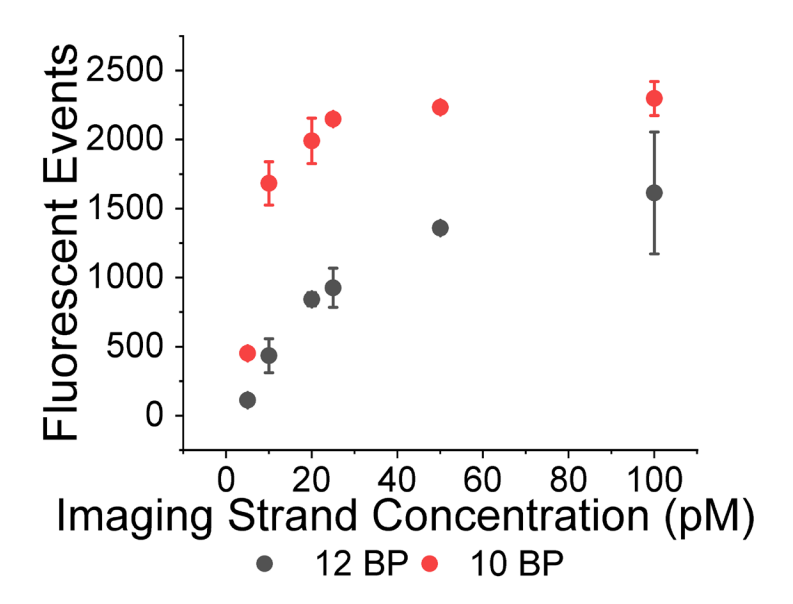


Figure 5: Fluorescent counts as a function of imaging strand concentration for different lengths of imaging strand DNA. Data points reflect the average of three repeat measurements at different regions of the same sample, with the error bars representing the standard deviation across those three measurements. Data was acquired over 1000 frames with a 200 ms integration time. Absence of error bars indicates that the standard deviation was on the order of the symbol size.

To demonstrate the temperature sensitivity of our nanothermometry approach, we constructed DNA melting curves by monitoring the number of fluorescent events as a function of temperature.

For these samples, the anchor strand was hybridized with a 36 BP blocking strand and then exposed to heated 0.3X PBS buffer solution for 10 minute segments at increasing temperatures. After each *ex situ* heating cycle, three regions of the sample were imaged with DNA-PAINT to obtain counting statistics on the number of fluorescence events. Temperature measurements were performed in order, since the DNA denaturation process only reports on the highest temperature experienced by the system, unless blocking strand is reintroduced (as in **Figure 3**). **Figure 6** shows the resulting melting curve, where the number of events at each temperature is normalized by the maximum number of events when $T >> T_m$. For this set of conditions, we found that temperatures above 58° C are sufficient to remove all the blocking strand.

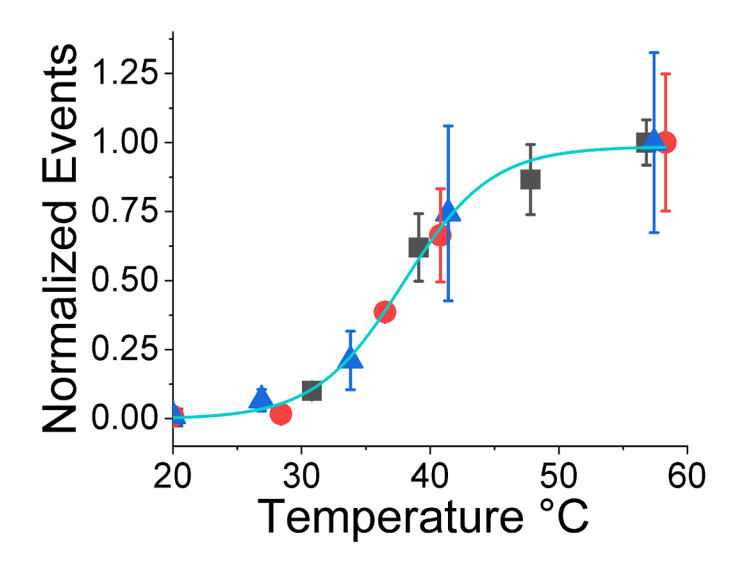


Figure 6: DNA-PAINT melting curve using 48 BP anchor strand, 36 BP blocking strand and 0.3X PBS melting buffer, imaged with 10 pM 10 BP imaging strand in 2.0X PBS + 600 mM NaCl. The red, blue, and black data points correspond to different experiments done on different days by multiple researchers. The number of events has been normalized to the maximum number of events when $T >> T_m$ (here $\approx 58^{\circ}$ C). Data points are averages of three repeat measurements at different regions of interest on the sample, with the error bars representing the standard deviation. The data was fit to Equation 1 and the experimental melting temperature (T_m) was determined to be 38°C for these blocking and melting conditions. The blocking efficiency is calculated to be 99.6% +/-0.4.

The resultant curve shown in **Figure 6** is an aggregated data set from multiple samples produced by different researchers and imaged on different days. We found that each sample had different maximum numbers of binding events when fully unblocked (e.g. at high T, Table S1), which could be due to variability in gold surface area (e.g. defects in the array), Au-S functionalization efficiency, and/or DNA surface density. However, as we moved to different regions of a given sample, we found better site-to-site reproducibility, suggesting that the DNA functionalization step is the most likely contributor to variations in total events, since we would not expect defects in the array to persist over the entire sample. Because we also obtain super-resolved data with our technique, we examined the events from each region of interest under a given set of conditions and found that each nanotriangle shows roughly the same number of events (representative data shown in Figure S5), further supporting our conclusion that the functionalization is uniform across the sample, even though it may vary from sample-to-sample. Importantly, upon normalizing the temperature-dependent activity for each experiment by its maximum counts at high temperature, we find that they all lie along the same master curve, allowing us to conclude that the differences in DNA density does not appear to have a negative effect on the temperature response of the system.

We fit the data in **Figure 6** to the following equation, where F is the normalized number of fluorescence counts at a given temperature, F_{max} is the maximum value of our normalized fluorescence counts, F_{min} is the minimum value of normalized fluorescence counts, T is the temperature, T_m is the melting temperature, and dT is the steepness of the curve around T_m :

$$F(T) = F_{max} + \frac{(F_{min} - F_{max})}{\left(1 + \exp\left(\frac{(T - T_m)}{dT}\right)\right)} \tag{1}$$

The data in **Figure 6** is well described by equation 1, yielding a T_m value of 38°C. The sample-to-sample agreement showcases the reproducibility of using normalized counts as a measure of the available anchor strands on the gold nanoparticle surface.

Next, we tested the tunability of the temperature sensitivity of our approach. DNA melting temperatures strongly depend upon the number of hybridized base pairs, the sequence of those base pairs, and the salinity of the environment under which melting occurs. 48,49 This dependence provides us many opportunities to tune the temperature ranges over which we can interrogate with this new nanothermometry technique. After the success of the first melting curve using a 36 BP blocking strand and 0.3X PBS (shown in Figure 6 and reproduced in Figure 7A, light blue), we altered the melting temperature of the duplex by changing the salinity of the buffer used during heating. In Figure 7A, the red data shows that by increasing the salinity of the melting buffer to 1.0X PBS, we increased the experimentally determined T_m of the 36 BP blocking strand from 38°C to 54°C. We compared the experimental melting curves to those predicted by uMelt, a solution phase melting curve predictive software.⁴⁸ uMelt predicted a 10° increase in the melting temperature as we increased the salinity from 0.3 to 1.0X PBS, agreeing reasonably well with our experimentally measured increase of 16° C. Although the agreement between the T_m values measured by DNA-PAINT (38° and 54°C) and those predicted by uMelt (54° and 64°C) differ significantly, we were unsurprised by this result, given that the calculations are done in solution phase (and are typically not considered to be as accurate for smaller oligomers), 50-52 while our experiments were performed with DNA monolayers on the nanoparticle surface. Thus, we consider uMelt as a helpful tool for making predictions regarding trends in DNA melting temperatures, even if the values do not agree exactly.

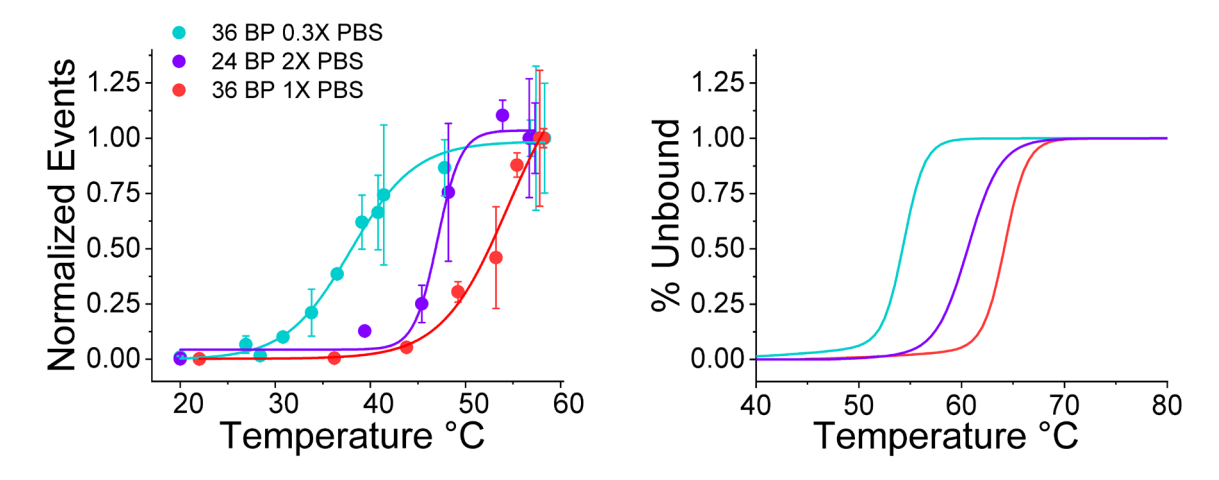


Figure 7: (A) Experimental DNA-PAINT melting curves using various blocking strand lengths and melting buffer salt concentrations (as shown in the legend). Each experiment used 48 BP anchor strand and 10 pM 10 BP imaging strand in 2.0X PBS + 600 mM NaCl buffer. Each data set was fit to a sigmoid, and the experimental melting temperature (T_m) was extracted. Extracted melting temperatures: Blue $T_m = 38^{\circ}$ C, purple $T_m = 47^{\circ}$ C, and red $T_m = 54^{\circ}$ C. (B) Theoretical melting curves for the same sequences and salinity conditions as in (A). The trend in the melting temperatures matches the experimental data, although the T_m values differ, most likely due to differences in the conditions (surface-bound vs. solution). Blue $T_m = 54^{\circ}$ C, purple $T_m = 61^{\circ}$ C, and red $T_m = 64^{\circ}$ C.

To test this idea, we switched to a 24 BP blocking strand and used uMelt to predict a melt buffer salinity that would yield a T_m value between the two that we had already measured. The predicted curve is shown in **Figure 7B** (purple) for a 24 BP blocking strand in 2.0X PBS melt buffer. We then proceeded to build an experimental melting curve from samples under these conditions (**Figure 7A**, purple), and found that the result matched well with what was predicted from theory. Interestingly, we experimentally observed that the melting transition is sharper for the shorter blocking strand, in direct contrast to the theoretical prediction. Future plans include a systematic study of how different heating conditions impact not only the melting temperature but also the shape of the DNA melting curves. Nonetheless, despite these differences between experiment and theory, we have clearly demonstrated the ability to tune the temperature sensitivity of our DNA-

PAINT based nanothermometry approach by modifying the DNA sequence and/or buffer salinity. Thus, by functionalizing a sample with a carefully designed DNA duplex and measuring the ratio in fluorescence activity between the sample at an unknown temperature and at a temperature well above T_m , we believe our approach makes it possible to extract quantitative temperature information.

One challenge with our approach is that it is useful to have a sense of the expected temperature that the surface will reach, in order to design the appropriate DNA sequence and salinity conditions to tune the melting curve into the appropriate regime. However, this is not an insurmountable barrier, as trial-and-error will allow the correct conditions to be found, albeit at a potentially significant cost. Numerical solutions of the steady-state or time-dependent heat diffusion equation can also be used to approximate the temperature at the nanoscale. ^{37,53} An additional challenge lies in the comparison between bulk solution-phase heating (which we have done here) and photothermal heating. In our current experiments, the DNA melting occurred when the system has a large volume of solution at a near-uniform temperature, while we expect photothermal heating to have gradient differences in temperature between the near surface and bulk solution. This situation may alter the DNA melting behavior due to near-surface terminal unzipping, lowering the overall stability of the duplex and shifting T_m to lower values.^{54,55} In future experiments, we will compare how the length of the anchor strand and the position/length of the blocking strand affects the melting behavior in both solution phase and photothermal heating experiments.

We also note that this technique only reports on the highest temperature the system has experienced, rather than providing a real time, *in situ* readout of the temperature. This *in situ* temperature restriction is due to the nature of the DNA-PAINT process, which relies on a transient,

yet sufficiently long-lived, interaction between the anchor strand and the imaging strand that would fail to occur at temperatures exceeding the melting temperature of the anchor-imager duplex. Moreover, in order for DNA-PAINT to generate enough fluorescent events to be statistically relevant for extracting a quantitative temperature, we need to image the system for a sufficient length of time in order to collect enough data. For the multi-particle temperature experiments presented here, we took 1000 frames with 200 ms integration times, for a total imaging time of 200 s; this timing was sufficient to generate statistics to measure the temperature of the system, but did not yield high quality super-resolved images of the individual nanoparticles (Figure S5). For measurements on single particles, longer imaging times would be required to generate enough binding events to be statistically significant (as in Figure 2B). While the extended imaging time is a limitation of the technique for in situ temperature measurements, this issue is offset by the well-established ability of DNA-PAINT to generate super-resolved images. In particular, this advantage is crucial for probing non-uniform thermal profiles in nanoparticle assemblies, where the ability to measure temperature in real time is far less critical than probing quantitative differences in the thermal properties of the individual nanoparticles, as will be demonstrated in future work. ³⁹

Beyond the ability to achieve super-resolved images, an additional advantage of our approach is that a temperature can be checked by simply changing the blocking strand identity and/or salinity during the melting process. For example, **Figure 7A** shows that all three conditions we tested yield a different, but measurable, response at 47°C, suggesting that multiple measurements can improve the accuracy of the experimentally-measured temperature. One additional advantage of our approach is that heating and readout occur separately, as demonstrated by the *ex situ* measurements presented herein. We can therefore design the system to ensure that the act of

interrogating the imaging strand does not also impact the local heating. For example, as the data in **Figure S3** shows, we could use an IR laser to excite our nanotriangles on resonance and generate photothermal heating at their surfaces, and then separately use a non-resonant green laser (as we did here) to probe the imaging strand and determine the effects of photothermal heating. We can

also change the fluorophore tag on the imaging strand if we need to use a different readout laser.

The modularity of this approach allows a degree of control that provides both opportunities for

optimization as well as measurement redundancy, leading to improved accuracy.

CONCLUSION

In summary, we present progress towards a super-resolution nanothermometry technique that exploits the well-defined temperature-dependent melting of DNA to provide an indirect readout of local temperature at the nanoscale. By combining DNA-PAINT with surface-tethered DNA duplexes with controllable melting characteristics, we are able to generate melting curves by counting single molecule fluorescence binding events. We are able to control the temperature sensitivity of the measurement by tuning the melting temperature of the DNA through adjusting

the base pair length and salinity of the solution used during heating. Ultimately, this tunability

provides the control necessary to explore a wide range of samples and solution conditions,

allowing the study of various photothermally-heated systems.

ASSOCIATED CONTENT

ABBREVIATIONS

PBS, phosphate buffered saline, BP, base pair

20

Supporting Information.

The following files are available free of charge. Detailed methods, microscope and heating setup, theoretical calculations of nanoparticle absorption, and accompanying graphics (PDF)

AUTHOR INFORMATION

Corresponding Author

Email* kwillets@temple.edu

ACKNOWLEDGMENT

The authors would like to thank Dr. Stephen Lee (Rice University) for his help with SMALL-LABS, as well as Zachary Dwight (University of Utah) for his help with the UMelt software.

Funding Sources

This work was supported by the U.S. National Science Foundation under grant nos. NSF CHE-1728340 and CHE-2118389 (K.A.W.); CHE-1727122 and CHE-2118420 (S.L); and CHE-1727092 and CHE-2118333 (D.J.M.). S.L. also acknowledges support from the Charles W. Duncan, Jr.-Welch Chair in Chemistry (C-0002).

REFERENCES

(1) Odom, T. W.; Schatz, G. C. Introduction to Plasmonics. *Chemical Reviews* **2011**, *111* (6), 3667–3668

- (2) Kuppe, C.; Rusimova, K. R.; Ohnoutek, L.; Slavov, D.; Valev, V. K. "Hot" in Plasmonics: Temperature-Related Concepts and Applications of Metal Nanostructures. *Advanced Optical Materials* **2020**, *8* (1), 1901166
- (3) Brongersma, M. L.; Halas, N. J.; Nordlander, P. Plasmon-Induced Hot Carrier Science and Technology. *Nature Nanotechnology* **2015**, *10* (1), 25–34
- (4) Neumann, O.; Urban, A. S.; Day, J.; Lal, S.; Nordlander, P.; Halas, N. J. Solar Vapor Generation Enabled by Nanoparticles. *ACS Nano* **2012**, *7* (1), 42–49
- (5) Govorov, A. O.; Richardson, H. H. Generating Heat with Metal Nanoparticles. *Nano Today* **2007**, *2* (1), 30–38
- (6) Baffou, G.; Quidant, R.; Abajo, F. J. G. de. Nanoscale Control of Optical Heating in Complex Plasmonic Systems. *ACS Nano* **2010**, *4* (2), 709–716
- (7) Govorov, A. O.; Zhang, W.; Skeini, T.; Richardson, H.; Lee, J.; Kotov, N. A. Gold Nanoparticle Ensembles as Heaters and Actuators: Melting and Collective Plasmon Resonances. *Nanoscale Research Letters* **2006**, *1* (1), 84-90
- (8) Zhou, N.; Xu, X.; Hammack, A. T.; Stipe, B. C.; Gao, K.; Scholz, W.; Gage, E. C. Plasmonic Near-Field Transducer for Heat-Assisted Magnetic Recording. *Nanophotonics* **2014**, *3* (3), 141–155
- (9) Bello, F.; Sanvito, S.; Hess, O.; Donegan, J. F. Shaping and Storing Magnetic Data Using Pulsed Plasmonic Nanoheating and Spin-Transfer Torque. *ACS Photonics* **2019**, *6* (6), 1524–1532
- (10) Gosciniak, J.; Rasras, M. High Field Enhancement between Transducer and Resonant Antenna for Application in Bit Patterned Heat-Assisted Magnetic Recording. *Optics Express* **2019**, *27* (6), 8605–8611
- (11) Jain, P. K.; Huang, X.; El-Sayed, I. H.; El-Sayed, M. A. Noble Metals on the Nanoscale: Optical and Photothermal Properties and Some Applications in Imaging, Sensing, Biology, and Medicine. *Accounts of Chemical Research* **2008**, *41* (12), 1578–1586
- (12) Rastinehad, A. R.; Anastos, H.; Wajswol, E.; Winoker, J. S.; Sfakianos, J. P.; Doppalapudi, S. K.; Carrick, M. R.; Knauer, C. J.; Taouli, B.; Lewis, S. C.; et al. Gold Nanoshell-Localized Photothermal Ablation of Prostate Tumors in a Clinical Pilot Device Study. *Proceedings of the National Academy of Sciences* **2019**, *116* (37), 18590–18596
- (13) Kennedy, L. C.; Bickford, L. R.; Lewinski, N. A.; Coughlin, A. J.; Hu, Y.; Day, E. S.; West, J. L.; Drezek, R. A. A New Era for Cancer Treatment: Gold-Nanoparticle-Mediated Thermal Therapies. *Small* 2011, 7 (2), 169–183
- (14) Blanco, E.; Shen, H.; Ferrari, M. Principles of Nanoparticle Design for Overcoming Biological Barriers to Drug Delivery. *Nature Biotechnology* **2015**, *33* (9), 941–951

- (15) Everts, M.; Saini, V.; Leddon, J. L.; Kok, R. J.; Stoff-Khalili, M.; Preuss, M. A.; Millican, L. C.; Perkins, G.; Brown, J. M.; Bagaria, H.; et al. Covalently Linked Au Nanoparticles to a Viral Vector: Potential for Combined Photothermal and Gene Cancer Therapy. *Nano Letters* **2006**, *6* (4), 587–591
- (16) Kumar, R.; Maitra, A. N.; Patanjali, P. K.; Sharma, P. Hollow Gold Nanoparticles Encapsulating Horseradish Peroxidase. *Biomaterials* **2005**, *26* (33), 6743–6753
- (17) Lee, J.; Mubeen, S.; Ji, X.; Stucky, G. D.; Moskovits, M. Plasmonic Photoanodes for Solar Water Splitting with Visible Light. *Nano Letters* **2012**, *12* (9), 5014–5019
- (18) Robatjazi, H.; Bahauddin, S. M.; Doiron, C.; Thomann, I. Direct Plasmon-Driven Photoelectrocatalysis. *Nano Letters* **2015**, *15* (9), 6155–6161
- (19) Cortés, E.; Besteiro, L. v.; Alabastri, A.; Baldi, A.; Tagliabue, G.; Demetriadou, A.; Narang, P. Challenges in Plasmonic Catalysis. *ACS Nano* **2020**, *14* (12), 16202–16219
- (20) Yu, S.; Wilson, A. J.; Kumari, G.; Zhang, X.; Jain, P. K. Opportunities and Challenges of Solar-Energy-Driven Carbon Dioxide to Fuel Conversion with Plasmonic Catalysts. *ACS Energy Letters* **2017**, *2* (9), 2058–2070
- (21) Yu, Y.; Sundaresan, V.; Willets, K. A. Hot Carriers versus Thermal Effects: Resolving the Enhancement Mechanisms for Plasmon-Mediated Photoelectrochemical Reactions. *The Journal of Physical Chemistry C* **2018**, *122* (9), 5040–5048
- (22) Wilson, A. J.; Mohan, V.; Jain, P. K. Mechanistic Understanding of Plasmon-Enhanced Electrochemistry. *The Journal of Physical Chemistry C* **2019**, *123* (48), 29360–29369
- (23) Hoener, B. S.; Kirchner, S. R.; Heiderscheit, T. S.; Collins, S. S. E.; Chang, W. S.; Link, S.; Landes, C. F. Plasmonic Sensing and Control of Single-Nanoparticle Electrochemistry. *Chem* **2018**, *4* (7), 1560–1585
- (24) Barella, M.; Violi, I. L.; Gargiulo, J.; Martinez, L. P.; Goschin, F.; Guglielmotti, V.; Pallarola, D.; Schlücker, S.; Pilo-Pais, M.; Acuna, G. P.; et al. In Situ Photothermal Response of Single Gold Nanoparticles through Hyperspectral Imaging Anti-Stokes Thermometry. *ACS Nano* **2020**, *15* (2), 2458–2467
- (25) Carattino, A.; Caldarola, M.; Orrit, M. Gold Nanoparticles as Absolute Nanothermometers. *Nano Letters* **2018**, *18* (2), 874–880
- (26) Keller, E. L.; Frontiera, R. R. Ultrafast Nanoscale Raman Thermometry Proves Heating Is Not a Primary Mechanism for Plasmon-Driven Photocatalysis. *ACS Nano* **2018**, *12* (6), 5848–5855

- (27) Pozzi, E. A.; Zrimsek, A. B.; Lethiec, C. M.; Schatz, G. C.; Hersam, M. C.; Duyne, R. P. van. Evaluating Single-Molecule Stokes and Anti-Stokes SERS for Nanoscale Thermometry. *Journal of Physical Chemistry C* **2015**, *119* (36), 21116–21124
- (28) Lin, K.-Q.; Yi, J.; Zhong, J.-H.; Hu, S.; Liu, B.-J.; Liu, J.-Y.; Zong, C.; Lei, Z.-C.; Wang, X.; Aizpurua, J.; et al. Plasmonic Photoluminescence for Recovering Native Chemical Information from Surface-Enhanced Raman Scattering. *Nature Communications* **2017**, *8* (1), 1–9
- (29) Jiang, Q.; Rogez, B.; Claude, J.-B.; Baffou, G.; Wenger, J. Temperature Measurement in Plasmonic Nanoapertures Used for Optical Trapping. *ACS Photonics* **2019**, *6* (7), 1763–1773
- (30) Lee, M. H.; Lin, H. Y.; Yang, C. N. A DNA-Based Two-Way Thermometer to Report High and Low Temperatures. *Analytica Chimica Acta* **2019**, *1081*, 176–183
- (31) Wu, Y.; Liu, J.; Wang, Y.; Li, K.; Li, L.; Xu, J.; Wu, D. Novel Ratiometric Fluorescent Nanothermometers Based on Fluorophores-Labeled Short Single-Stranded DNA. ACS Applied Materials and Interfaces 2017, 9 (12), 11073–11081
- (32) Bu, C.; Mu, L.; Cao, X.; Chen, M.; She, G.; Shi, W. DNA Nanostructure-Based Fluorescence Thermometer with Silver Nanoclusters. *Nanotechnology* **2018**, *29* (29), 295501
- (33) Gareau, D.; Desrosiers, A.; Vallée-Bélisle, A. Programmable Quantitative DNA Nanothermometers. *Nano Letters* **2016**, *16* (7), 3976–3981
- (34) Ebrahimi, S.; Akhlaghi, Y.; Kompany-Zareh, M.; Rinnan, S. Nucleic Acid Based Fluorescent Nanothermometers. **2021**, *41*, 46.
- (35) You, M.; Jia, P.; He, X.; Wang, Z.; Feng, S.; Ren, Y.; Li, Z.; Cao, L.; Gao, B.; Yao, C.; et al. Quantifying and Adjusting Plasmon-Driven Nano-Localized Temperature Field around Gold Nanorods for Nucleic Acids Amplification. *Small Methods* **2021**, 5 (5), 2001254
- (36) Hastman, D. A.; Melinger, J. S.; Aragonés, G. L.; Cunningham, P. D.; Chiriboga, M.; Salvato, Z. J.; Salvato, T. M.; Carl W.; Brown, I.; Mathur, D.; et al. Femtosecond Laser Pulse Excitation of DNA-Labeled Gold Nanoparticles: Establishing a Quantitative Local Nanothermometer for Biological Applications. *ACS Nano* **2020**, 14 (7), 8570–8583
- (37) Baldwin, C. L.; Bigelow, N. W.; Masiello, D. J. Thermal Signatures of Plasmonic Fano Interferences: Toward the Achievement of Nanolocalized Temperature Manipulation. *Journal of Physical Chemistry Letters* **2014**, *5* (8), 1347–1354
- (38) Jebeli, S. A. H.; West, C. A.; Lee, S. A.; Goldwyn, H. J.; Bilchak, C. R.; Fakhraai, Z.; Willets, K. A.; Link, S.; Masiello, D. J. Wavelength-Dependent Photothermal Imaging Probes Nanoscale Temperature Differences among Subdiffraction Coupled Plasmonic Nanorods. *Nano Letters* **2021**, *21* (12), 5386–5393

- (39) Bhattacharjee, U.; West, C. A.; Jebeli, S. A. H.; Goldwyn, H. J.; Kong, X.-T.; Hu, Z.; Beutler, E. K.; Chang, W.-S.; Willets, K. A.; Link, S. et al. Active Far-Field Control of the Thermal Near-Field via Plasmon Hybridization. *ACS Nano* **2019**, *13* (8), 9655–9663
- (40) Jungmann, R.; Steinhauer, C.; Scheible, M.; Kuzyk, A.; Tinnefeld, P.; Simmel, F. C. Single-Molecule Kinetics and Super-Resolution Microscopy by Fluorescence Imaging of Transient Binding on DNA Origami. *Nano Letters* 2010, 10 (11), 4756–4761
- (41) Taylor, A.; Verhoef, R.; Beuwer, M.; Wang, Y.; Zijlstra, P. All-Optical Imaging of Gold Nanoparticle Geometry Using Super-Resolution Microscopy. *Journal of Physical Chemistry C* **2018**, *122* (4), 2336–2342
- (42) Hulteen, J. C.; Duyne, R. P. van. Nanosphere Lithography: A Materials General Fabrication Process for Periodic Particle Array Surfaces. *Journal of Vacuum Science & Technology A: Vacuum, Surfaces, and Films* **1998**, *13* (3), 1553
- (43) Zhang, X.; Servos, M. R.; Liu, J. Instantaneous and Quantitative Functionalization of Gold Nanoparticles with Thiolated DNA Using a PH-Assisted and Surfactant-Free Route. *Journal of the American Chemical Society* **2012**, *134* (17), 7266–7269
- (44) Hurst, S. J.; Lytton-Jean, A. K. R.; Mirkin, C. Maximizing DNA Loading on a Range of Gold Nanoparticle Sizes. *Analytical Chemistry* **2006**, *78* (24), 8313–8318
- (45) Cheng, X.; Anthony, T. P.; West, C. A.; Hu, Z.; Sundaresan, V.; McLeod, A. J.; Masiello, D. J.; Willets, K. A. Plasmon Heating Promotes Ligand Reorganization on Single Gold Nanorods. *The Journal of Physical Chemistry Letters* **2019**, *10* (6), 1394–1401
- (46) Blumhardt, P.; Stein, J.; Mücksch, J.; Stehr, F.; Bauer, J.; Jungmann, R.; Schwille, P. Photo-Induced Depletion of Binding Sites in DNA-PAINT Microscopy. *Molecules* **2018**, *23* (12), 3165
- (47) Isaacoff, B. P.; Li, Y.; Lee, S. A.; Biteen, J. S. SMALL-LABS: Measuring Single-Molecule Intensity and Position in Obscuring Backgrounds. *Biophysical Journal* 2019, 116 (6), 975–982
- (48) Dwight, Z.; Palais, R.; Wittwer, C. T. UMELT: Prediction of High-Resolution Melting Curves and Dynamic Melting Profiles of PCR Products in a Rich Web Application. *Bioinformatics* **2011**, *27* (7), 1019–1020
- (49) Huguet, J. M.; Bizarro, C. v.; Forns, N.; Smith, S. B.; Bustamante, C.; Ritort, F. Single-Molecule Derivation of Salt Dependent Base-Pair Free Energies in DNA. *Proceedings of the National Academy of Sciences* **2010**, *107* (35), 15431–15436
- (50) Nasef, H.; Ozalp, V. C.; Beni, V.; O'Sullivan, C. K. Melting Temperature of Surface-Tethered DNA. *Analytical Biochemistry* **2010**, *406* (1), 34–40

- (51) Qamhieh, K.; Wong, K.; Lynch, G. C.; Pettitt, B. M. THE MELTING MECHANISM OF DNA TETHERED TO A SURFACE. *International journal of numerical analysis and modeling* **2009**, *6* (3), 474.
- (52) Panjkovich, A.; Melo, F. Comparison of Different Melting Temperature Calculation Methods for Short DNA Sequences. *Bioinformatics* **2005**, *21* (6), 711–722
- (53) Aleshire, K.; Pavlovetc, I. M.; Collette, R.; Kong, X.-T.; Rack, P. D.; Zhang, S.; Masiello, D. J.; Camden, J. P.; Hartland, G.; Kuno, M. Far-Field Midinfrared Superresolution Imaging and Spectroscopy of Single High Aspect Ratio Gold Nanowires. *Proceedings of the National Academy of Sciences* 2020, 117 (5), 2288–2293
- (54) Santosh, M.; Maiti, P. K. Force Induced DNA Melting. *Journal of Physics Condensed Matter* **2009**, *21* (3) 034113
- (55) Harris, N. C.; Kiang, C.-H. Defects Can Increase the Melting Temperature of DNA-Nanoparticle Assemblies. *The Journal of Physical Chemistry B* **2006**, *110* (33), 16393

TOC Graphic

